Article

Simultaneously Wavelength- and Temperature-Insensitive Mid-Infrared Optical Parametric Amplification with LiGaS$_2$ Crystal

Zhixuan Hu [ID] and Jingui Ma *[ID]

Key Laboratory for Laser Plasmas (Ministry of Education), Collaborative Innovation Centre of IFSA (CICIFSA), School of Physics and Astronomy, Shanghai Jiao Tong University, Shanghai 200240, China; huzhixuan@sjtu.edu.cn
* Correspondence: majg@sjtu.edu.cn

Abstract: Ultrafast mid-infrared (mid-IR) lasers with a high pulse repetition rate are in great demand in various fields, including attosecond science and strong-field physics. Due to the lack of suitable mid-IR laser gain medium, optical parametric amplifiers (OPAs) are used to generate an ultrafast mid-IR laser. However, the efficiency of OPA is sensitive to phase mismatches induced by wavelength and temperature deviations from the preset points, which thus limits the pulse duration and the average power of the mid-IR laser. Here, we exploited a noncollinear phase-matching configuration to achieve simultaneously wavelength- and temperature-insensitive mid-IR OPA with a LiGaS$_2$ crystal. The noncollinearity can cancel the first-order dependence of phase matching on both wavelength and temperature. Benefitting from the thermal property of the LiGaS$_2$ crystal, some collinear phase-matching solutions derived from the first-order and even third-order wavelength insensitivity have comparatively large temperature bandwidths and can be regarded as approximate solutions with simultaneous wavelength and temperature insensitivity. These simultaneously wavelength- and temperature-insensitive phase-matching designs are verified through numerical simulations in order to generate few-cycle, high-power mid-IR pulses.

Keywords: mid-infrared lasers; ultrafast lasers; optical parametric amplification; LiGaS$_2$ crystal

1. Introduction

Mid-infrared (mid-IR) lasers are important for the fields of research, industry, and medicine. In particular, ultrafast intense mid-IR lasers are in great demand in attosecond science due to the λ^2-scaling law in the high-order harmonic generation (HHG) process (cutoff frequency $\propto \lambda^2$, pulse duration $\propto \lambda^{-2}$) [1]. Mid-IR laser-driven HHG can generate shorter attosecond pulses with wavelengths accessible in both soft and hard X-ray regions [2]. However, compared with generating visible and near-IR lasers directly from laser oscillators or amplifiers that are well developed and even commercialized, the generation of mid-IR lasers is much more difficult due to the lack of suitable laser gain materials, especially in the range beyond 3 μm [3]. Therefore, nonlinear optical parametric amplification (OPA) has become the popular route for generating mid-IR lasers [4,5]. Different from laser amplifiers, OPA has to satisfy the phase-matching (PM) condition for efficient energy transfer from the pump to signal. PM is commonly enabled by the aid of birefringence in nonlinear crystals. However, the perfect PM condition is usually satisfied within a limited range of wavelengths and temperatures, as the refractive index depends on both the wavelength and temperature. The practical demands for ultrashort pulses and high repetition rates require a PM condition with both a large wavelength and temperature tolerance.

Nonlinear crystal plays a crucial role in mid-IR OPA. Generally speaking, it is difficult for oxide crystals to generate a mid-IR laser beyond 5 μm due to the limited infrared transparency; thus non-oxide semi-conductor crystals are used between 5 and 15 μm [6].

However, non-oxide crystals usually exhibit a stronger absorption than matured oxide crystals (e.g., at 2 μm: β-BBO, ~0.07 cm^{-1} [7]; LiGaS$_2$, ~0.47 cm^{-1} [8]; ZnGeP$_2$, ~0.15 cm^{-1} [7]). As near-IR OPAs with β-BBO crystals have suffered from a thermal effect under an average power of several tens of watts [9,10], the mid-IR OPA with non-oxide crystals will also face thermal issues in future high average power operations, although current low-power experiments have not encountered this problem [11–17].

In this study, we focus on the semiconductor LiGaS$_2$ crystal, which has been popular in recent years because it has a high transparency from 0.32 to 11.6 μm (at the 5 cm^{-1} absorption level), covering both the near-IR pump source around 1 μm and the mid-IR output beyond 10 μm [8]. Compared with other promising non-oxides (e.g., BaGa$_4$S$_7$), LiGaS$_2$ has a relatively large absorption across its transparent range. For example, the absorption coefficient at 1 μm is 0.51 cm^{-1} for LiGaS$_2$ [8], but <0.1 cm^{-1} for BaGa$_4$S$_7$ [18]. In addition, the effective nonlinear coefficient of LiGaS$_2$ is moderate (~5 pm·V^{-1} [19]), much lower than that of AgGaS$_2$ (~12 pm·V^{-1} [20]), BaGa$_4$Se$_7$ (~20 pm·V^{-1} [20]), and ZnGeP$_2$ (~70 pm·V^{-1} [7]). This means that a longer LiGaS$_2$ crystal may be needed to achieve efficient amplification, which not only sacrifices gain bandwidth, but also aggravates heat load. Therefore, it is necessary to develop PM with simultaneous wavelength and temperature insensitivity for future LiGaS$_2$-based high-power OPA processes. Unfortunately, there have been few studies on the thermal properties of PM in LiGaS$_2$ crystal, with very little consideration of simultaneous wavelength- and temperature-insensitive PM.

This article aims to reveal the possible PM solutions with simultaneous wavelength and temperature insensitivity for mid-IR OPA with LiGaS$_2$ crystals in both noncollinear and collinear PM configurations. By tuning the PM parameters such as signal wavelength and crystal temperature, the noncollinear angles corresponding to the wavelength-insensitive PM (WIPM) and temperature-insensitive PM (TIPM) can overlap, creating a simultaneous wavelength- and temperature-insensitive PM (WTIPM). Second-order and third-order WIPMs are found in LiGaS$_2$-based OPA. Interestingly, such high-order WIPMs also possess large temperature bandwidths, stemming from the good thermal properties of the LiGaS$_2$ crystal. Detailed design principles and all possible solutions for WTIPM will be introduced in Section 2 through theoretical analyses. In Section 3, the solutions of WTIPM and the third-order WIPM will be numerically applied to build mid-IR optical parametric chirped-pulse amplification (OPCPA), and the simulated large wavelength- and temperature- bandwidths will be used to validate the theoretical PM designs.

2. WTIPM Solutions for LiGaS$_2$-Based OPA

2.1. PM Design and Manipulation

In OPA, a low-frequency signal light (angular frequency ω_s) can be amplified by a high-frequency pump light (angular frequency ω_p, and $\omega_p > \omega_s$). Governed by the energy conservation law, an idler light is also generated in this process, with an angular frequency of $\omega_i = \omega_p - \omega_s$. Under the assumption that the pump cannot be depleted by conversion to the signal and idler, the small-signal gain that the signal light experiences is as follows [21]:

$$G = 1 + \frac{\Gamma^2}{g^2}\sinh^2(gL), \tag{1}$$

where $g = \sqrt{\Gamma^2 - \left(\frac{\Delta k}{2}\right)^2}$, $\Gamma^2 = \frac{2\omega_i\omega_s d_{eff}^2 I_p}{n_i n_s n_p \varepsilon_0 c^3}$, $\Delta k = k_p - k_s - k_i$ is the wave−vector mismatch and the k_j depends on the refractive index n_j by $k_j = n_j\omega_j/c$ (c is the light speed in vacuum), ε_0 is the permittivity of the vacuum, I_p is the pump intensity, and d_{eff} is the effective nonlinear coefficient. From Equation (1), the small-signal gain is maximized under a perfect PM condition (or momentum conservation condition), where $\Delta k = k_p - k_s - k_i = 0$. If the phase mismatch is large, the small-signal gain will decrease significantly. Hereinafter, the gain bandwidth ($\Delta\lambda$ denotes wavelength bandwidth, ΔT denotes temperature bandwidth) is defined as the full width at half maximum (FWHM) of the gain profile. The necessary PM environment can be created in a nonlinear crystal with the aid of birefringence.

In a broadband OPA, however, it is difficult to achieve the perfect PM condition for all the wavelength components because of the dispersion of the refractive index. Such a wavelength-dependent phase mismatch can be expressed by the Taylor expansion of Δk against the signal wavelength λ_s,

$$\Delta k = \Delta k_0 + \left.\frac{\partial \Delta k}{\partial \lambda_s}\right|_{\lambda_s=\lambda_{s0}} \Delta \lambda_s + \frac{1}{2}\left.\frac{\partial^2 \Delta k}{\partial \lambda_s^2}\right|_{\lambda_s=\lambda_{s0}} (\Delta \lambda_s)^2 + \frac{1}{6}\left.\frac{\partial^3 \Delta k}{\partial \lambda_s^3}\right|_{\lambda_s=\lambda_{s0}} (\Delta \lambda_s)^3 + O\left[(\Delta \lambda_s)^4\right], \quad (2)$$

where Δk_0 represents the phase mismatch among the central wavelength of three waves, and $\Delta \lambda_s = \lambda_s - \lambda_{s0}$ is the wavelength deviation from the central wavelength λ_{s0}. Normally, the condition of $\Delta k_0 = 0$ can be easily fulfilled by tuning the PM angle. To enlarge the wavelength bandwidth, the first-order derivative term in Equation (2) should be made zero,

$$\left.\frac{\partial \Delta k}{\partial \lambda_s}\right|_{\lambda=\lambda_{s0}} = 0. \quad (3)$$

This corresponds to the first-order WIPM condition. In this case, the wavelength bandwidth of PM is determined by the second-order derivative term in Equation (2). The first-order WIPM solutions can be found in collinear configuration and are only limited to several specific central wavelengths [12]. Instead, such first-order WIPM solutions are widespread under a noncollinear configuration (Figure 1b), because the noncollinear interaction introduces more degrees of freedom in the PM manipulation. Therefore, the noncollinear configuration has been widely adopted in broadband OPA and OPCPA systems [22–25].

As the refractive index of the nonlinear crystal is also a function of temperature, the PM condition becomes worse when there is a significant temperature rise in the nonlinear crystal under high-power operation. Similar to Equation (2), we can expand Δk against the crystal temperature T:

$$\Delta k = \Delta k_0 + \left.\frac{\partial \Delta k}{\partial T}\right|_{T=T_0} \Delta T + O\left[(\Delta T)^2\right], \quad (4)$$

where $\Delta T = T - T_0$ is the temperature deviation from the preset temperature T_0. The first-order TIPM condition can be expressed as,

$$\left.\frac{\partial \Delta k}{\partial T}\right|_{T=T_0} = 0. \quad (5)$$

In a collinear PM configuration, this condition may be fortunately satisfied under a specific wavelength in a specific crystal. Inspired by the noncollinear WIPM, some works have tried to realize TIPM using a noncollinear configuration in the near-IR OPA [26–28].

Furthermore, the WTIPM condition can be achieved if the first-order derivative terms of Δk in Equations (3) and (5) can both satisfy the following:

$$\left.\frac{\partial \Delta k}{\partial \lambda_s}\right|_{\lambda=\lambda_{s0}} = \left.\frac{\partial \Delta k}{\partial T}\right|_{T=T_0} = 0. \quad (6)$$

In this situation, a good PM condition can be ensured, even under large deviations of wavelength and temperature. However, the conditions given in Equation (6) are difficult to fulfill in a collinear configuration. Even in a noncollinear configuration, the noncollinear angles corresponding to the WIPM (Equation (3)) and TIPM (Equation (5)) are usually different from each other, so it is difficult to fulfill WTIPM by using single noncollinear angle α. To this end, more control degrees of freedom must be introduced, which means that the WTIPM may exist under appropriate combinations of multiple PM parameters, such as the noncollinear angle α, PM angle θ (or φ), pump wavelength λ_p, signal wavelength λ_s, and preset temperature T_0. For λ_p between 1 μm and 2 μm, we evaluated several widely

used mid-IR crystals (e.g., $AgGaS_2$, $AgGaSe_2$, $BaGa_4S_7$, $BaGa_4Se_7$, $ZnGeP_2$, and $LiGaS_2$) and found the WTIPM solution only in the $LiGaS_2$ crystal.

### 2.2. Collinear WTIPM Calculations

In the following PM calculations, the adopted Sellmeier equations and thermo-optic dispersion for the negative biaxial $LiGaS_2$ crystal were taken from [29]. According to these equations, we plotted the dependence of both the refractive index n and its first-order derivative against temperature $\partial n/\partial T$ on the wavelength from 1 to 10 μm, as shown in Figure 1c. As far as we know, all current nonlinear frequency conversions with $LiGaS_2$ crystal adopt a collinear PM (i.e., $\alpha = \Omega = 0$ in Figure 1b); thus, the collinear configuration was firstly evaluated for possible TWIPM solutions. We calculated the dispersions of both $\partial \Delta k/\partial \lambda_s$ and $\partial \Delta k/\partial T$ for a $LiGaS_2$-based OPA under both Type-I PM in the XZ plane and Type-II PM in the XY plane. The signal wavelengths were scanned from 3 to 10 μm. Two pump wavelengths of 1030 nm (Figure 2a) and 2060 nm (Figure 2b) were adopted, corresponding to the Yb-based and Ho-based high-power lasers, respectively. To show the wavelength and temperature tolerance, we also calculated the small-signal gain according to Equation (1) by tuning the wavelength and temperature, as shown in Figure 2c–f.

In the common pump case of $\lambda_p = 1030$ nm (Figure 2a), two WIPM solutions ($\partial \Delta k/\partial \lambda_s = 0$) were found at $\lambda_s = 7.8$ μm for Type-I PM and 8.6 μm for Type-II PM under the preset temperature of 323 K (50 °C). However, there was no TIPM solution ($\partial \Delta k/\partial T = 0$) in the studied signal wavelength range from 3 to 10 μm. Therefore, although large wavelength bandwidths of 1.25 μm ($\lambda_s = 7.8$ μm) and 1.2 μm ($\lambda_s = 8.6$ μm) could be achieved with the two WIPM solutions, their temperature bandwidths were limited to 72 K and 100 K, respectively (Figure 2c,d). As $\partial \Delta k/\partial T \neq 0$, the PM wavelength would change once the temperatures deviated from the preset temperatures. For the type-I PM in the XZ plane (Figure 2c), the PM wavelengths would shift from the WIPM solutions toward short-wavelength and long-wavelength directions with the increase in temperature, while the PM condition was no longer satisfied when the temperature was below the preset temperature. The type-II PM curve in the XY plane evolved in the opposite direction from the type-I PM in the XZ plane (Figure 2d), which originated from the opposite sign of $\partial \Delta k/\partial T$ for the two WIPM solutions. These calculations suggest that the current 1 μm-pumped OPA and OPCPA systems with the collinear WIPM solutions are not suitable in high average-power applications.
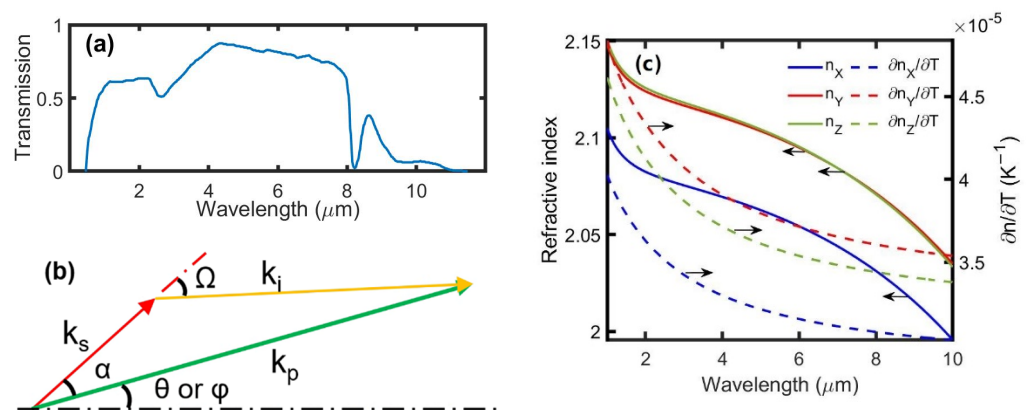
Figure 1. (**a**) Transmission spectrum of a 10 mm-thick $LiGaS_2$ crystal cited from the free SNLO software [8,30], which eliminated the influence from the Fresnel reflection. (**b**) Schematic for non-collinear PM in $LiGaS_2$ crystal. The k_p, k_s, and k_i are the wave-vectors of the pump, signal, and idler, respectively. The PM angle θ (φ) is defined by the angle between k_p and the crystal Z (X) axis in the XZ (XY) plane. The noncollinear angle α (Ω) refers to the angle between k_s and k_p (k_i). For collinear PM, $\alpha = \Omega = 0$. (**c**) Dispersion of the principle refractive index (solid) and the first-order derivative of principle refractive index against the temperature (dashed) of the $LiGaS_2$ crystal. Blue, red, and green curves refer to the parameters in the principle axes of X, Y, and Z, respectively.

In the other pump case of λ_p = 2060 nm (Figure 2b), the Type-I PM had a degenerate WIPM solution at λ_s = 4.12 μm, while the Type-II PM had a nondegenerate solution at λ_s = 6.5 μm. For the type-II PM in the XY plane, no TIPM solution existed (blue dashed curve in Figure 2b), meaning that the temperature bandwidth was limited (Figure 2f), similar to those in the 1 μm pump case. Surprisingly, the type-I PM in the XZ plane exhibited very broad temperature bandwidths, and the PM wavelengths only showed a slight shift when the temperature increased from the preset temperature to 200 °C, as shown in Figure 2e. This is because the WIPM solution of λ_s = 4.12 μm for the type-I PM in the XZ plane lay between two TIPM solutions of λ_s = 3.27 μm and 5.56 μm (red dashed curve in Figure 2b). As the value of $\partial \Delta k / \partial T$ at λ_s = 4.12 μm was also quite close to zero, such a collinear degenerate WIPM solution for the type-I PM in the XZ plane could be regarded as an equivalent WTIPM solution and could be chosen to build high-power mid-IR OPA and OPCPA.
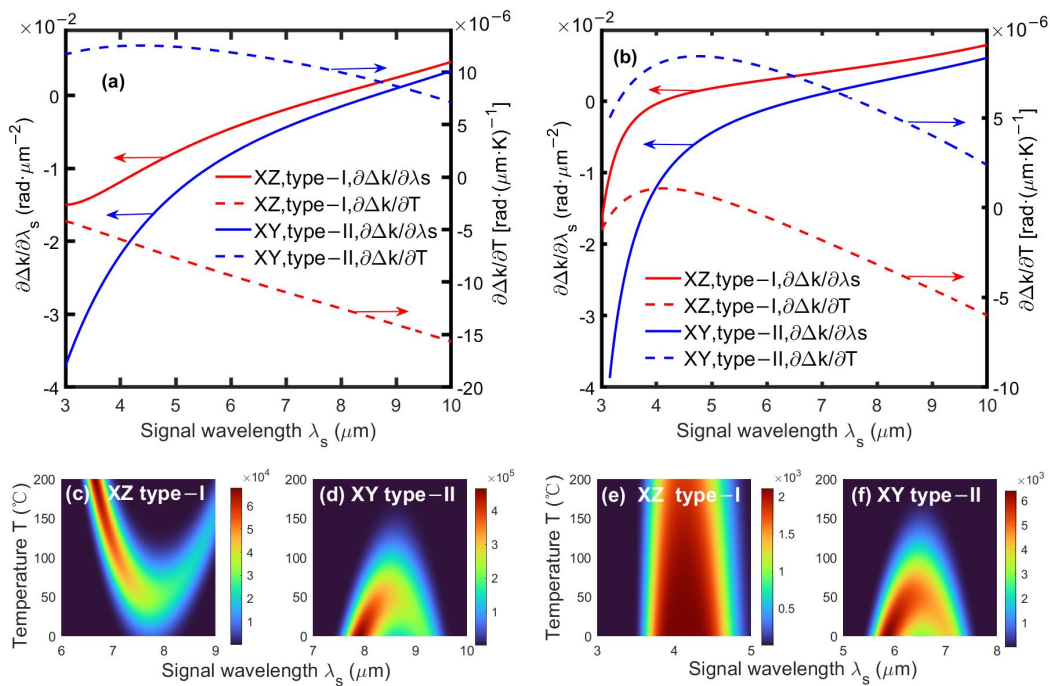

Figure 2. (**a**) Dependences of $\partial \Delta k / \partial \lambda_s$ (solid curves) and $\partial \Delta k / \partial T$ (dashed curves) on λ_s for a LiGaS$_2$-based collinear OPA with λ_p = 1.03 μm and T_0 = 323 K. Red curves, Type-I PM in the XZ plane; blue curves, Type-II PM in the XY plane. (**b**) Same as (**a**), but with λ_p = 2.06 μm. (**c–f**) Small-signal gain as a function of λ_s and temperature T with crystal length L = 10 mm and peak pump intensity I_p = 5 GW·cm^{-2}: (**c**) Type-I PM in XZ plane, λ_p = 1.03 μm, θ = 51.3°, φ = 0°, d_{eff} = 4.5 pm·V^{-1}; (**d**) Type-II PM in XY plane, λ_p = 1.03 μm, θ = 90°, φ = 36.8°, d_{eff} = 5.5 pm·V^{-1}; (**e**) Type-I PM in XZ plane, λ_p = 2.06 μm, θ = 53.8°, φ = 0°, d_{eff} = 4.7 pm·V^{-1}; (**f**) Type-II PM in XY plane, λ_p = 2.06 μm, θ = 90°, φ = 44.5°, d_{eff} = 5.5 pm·V^{-1}.

2.3. Noncollinear WTIPM Calculations

Here, we tried to find possible WTIPM solutions in a noncollinear OPA. In the collinear mid-IR OPA discussed in Section 2.2, the mid-IR light could either be seeded as a signal or generated as an idler because the two geometries were equivalent for the PM calculation. However, the two geometries were different in noncollinear OPA. If the mid-IR light was the idler of noncollinear OPA, it would be angularly dispersed. To avoid this, we only considered the noncollinear OPA geometry with the mid-IR light seeded as the signal. According to Equations (3) and (5), the noncollinear angle α could be used to achieve WIPM and TIPM, respectively; however, the two noncollinear angles are usually not equal. The WTIPM solution can only exist under some specific pump and signal wavelengths. Taking Type-I OPA in the XZ plane with λ_p = 2.06 μm as an example, we calculated the noncollinear

angles for WIPM and TIPM, respectively, as shown in Figure 3a. A WTIPM solution was found at λ_s = 5 μm, where WIPM and TIPM corresponded to the same noncollinear angle of ~2.9°. For other signal wavelengths, however, the WIPM and TIPM could not be fulfilled simultaneously under the same noncollinear angle. For the strict WTIPM solution, the OPA could provide a broad gain bandwidth from 4.6 to 5.6 μm, and could almost maintain the same gain, even when the temperature varied from 0 to 200 °C (Figure 3b). Such strict noncolinear WTIPM solutions exist in other pump wavelengths, as shown in Figure 3c,d. The WTIPM signal wavelength can be tuned from 2.16 to 2.35 μm (Figure 3c) and from 4.73 to 5.07 μm (Figure 3d) when the pump wavelength varies from 1.17 to 2.4 μm. Note that there is an end to the WTIPM solution at around λ_p = 1.53 μm, with the noncollinear angle α decreasing to 0 at this point. As α < 0 is nonsense, there was not any solution in the short-wavelength range when λ_p > 1.53 μm (Figure 3c) or in the long-wavelength range when λ_p < 1.53 μm (Figure 3d). As a result of their large temperature bandwidth, these WTIPM solutions were not sensitive to changes in the preset temperature, as shown in Figure 3c,d. The calculations in Figure 3 show the potential of noncollinear configuration in the design of high-power ultrafast mid-IR OPA and OPCPA.
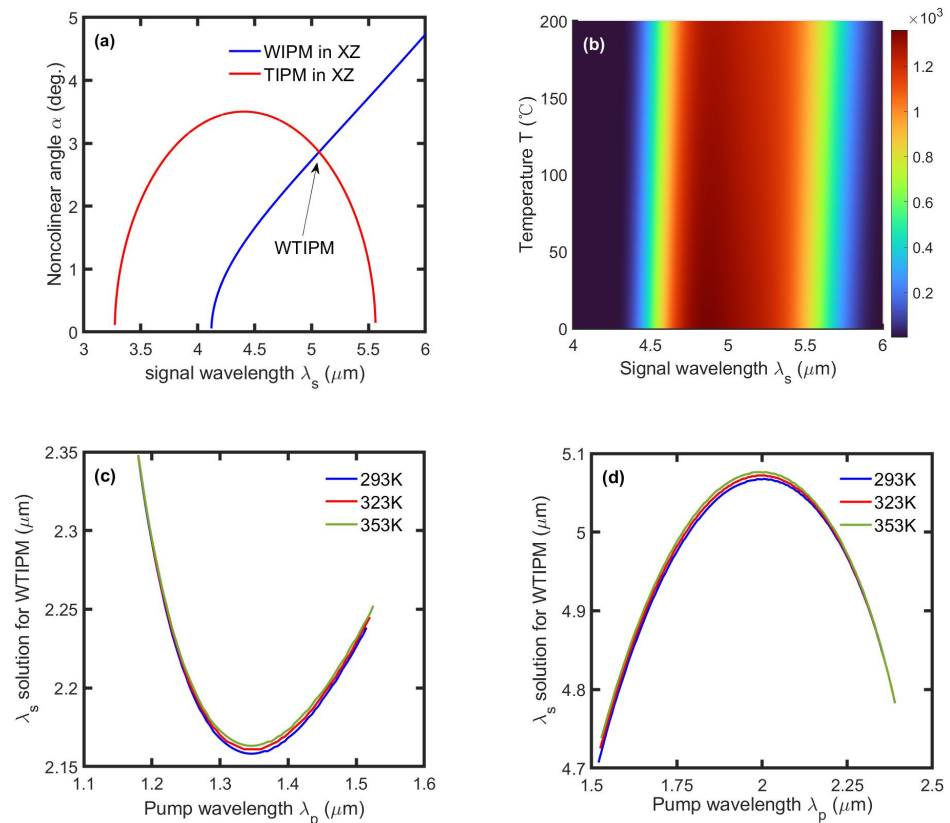
Figure 3. (**a**) Dispersion of a noncollinear angle corresponding to WIPM (blue curves) and TIPM (red curves) in a LiGaS$_2$-based OPA with λ_p = 2.06 μm, T_0 = 323 K. The intersection point (λ_s = 5 μm, α = 2.9°, θ = 50.9°, φ = 0, and d_{eff} = 4.5 pm·V^{-1}) represents the WTIPM solution. (**b**) Small-signal gain as a function of signal wavelength and temperature around the WTIPM point (**a**) with crystal length L = 10 mm and peak pump intensity I_p = 5 GW·cm^{-2}. (**c**) Signal wavelength solution for WTIPM when the pump wavelength varies from 1.17–1.53 μm. (**d**) Signal wavelength solution for WTIPM when the pump wavelength varies from 1.53–2.4 μm. Blue, red, and green curves represent the results at the preset temperatures of 293 K, 323 K, and 353 K, respectively.

According to Equation (2), the wavelength bandwidth may be further expanded if $\partial^2 \Delta k / \partial \lambda_s^2$ = 0 is also fulfilled on the basis of $\partial \Delta k / \partial \lambda_s$ = 0. We termed this PM second-order as WIPM. Usually, it is more difficult to achieve TIPM and second-order WIPM simultaneously, so we first explored the solution of second-order WIPM and then evaluated

its temperature bandwidth. In the common pump case of 1030 nm, we calculated the WIPM solutions (blue curve in Figure 4a) and their corresponding $\partial^2 \Delta k/\partial \lambda_s^2$ (red curve in Figure 4a). A second-order WIPM solution was found at $\lambda_s = 1.6$ μm. Interestingly, this solution also possessed a large temperature bandwidth of ~100 K, as shown in Figure 4c. Similar to the tuning of the WTIPM solution with a pump wavelength (as seen in Figure 3c,d), here, the second-order WIPM solution could also be tuned by varying the pump wavelength, as shown in Figure 4b. In the process of tuning, we also checked the value of $\partial^3 \Delta k/\partial \lambda_s^3$ and found a third-order WIPM solution ($\partial^3 \Delta k/\partial \lambda_s^3 = 0$) at $\lambda_p = 1.65$ μm and $\lambda_s = 3.3$ μm. This third-order WIPM solution was actually a collinear solution because the noncollinear angle became zero. This corresponds to the famous case of critical wavelength degeneracy ($\lambda_s = 2\lambda_p$) [25], in which all odd-order derivative terms in Equation (2) are eliminated. As a result, the wavelength bandwidth could be as large as ~2 μm around $\lambda_s = 3.3$ μm; interestingly, the temperature bandwidth was also quite large (Figure 4d). The large temperature bandwidth for the third-order WIPM was due to the thermal properties of the LiGaS$_2$ crystal. Therefore, the third-order WIPM solution could also be regarded as an approximate WTIPM solution. In practice, the use of this collinear solution for third-order WIPM, a small noncollinear angle (~0.5°) between the pump, and signal beams should be introduced to split the signal and idler after OPA. This small-angle noncollinearity would not have a significant effect on the signal amplification.
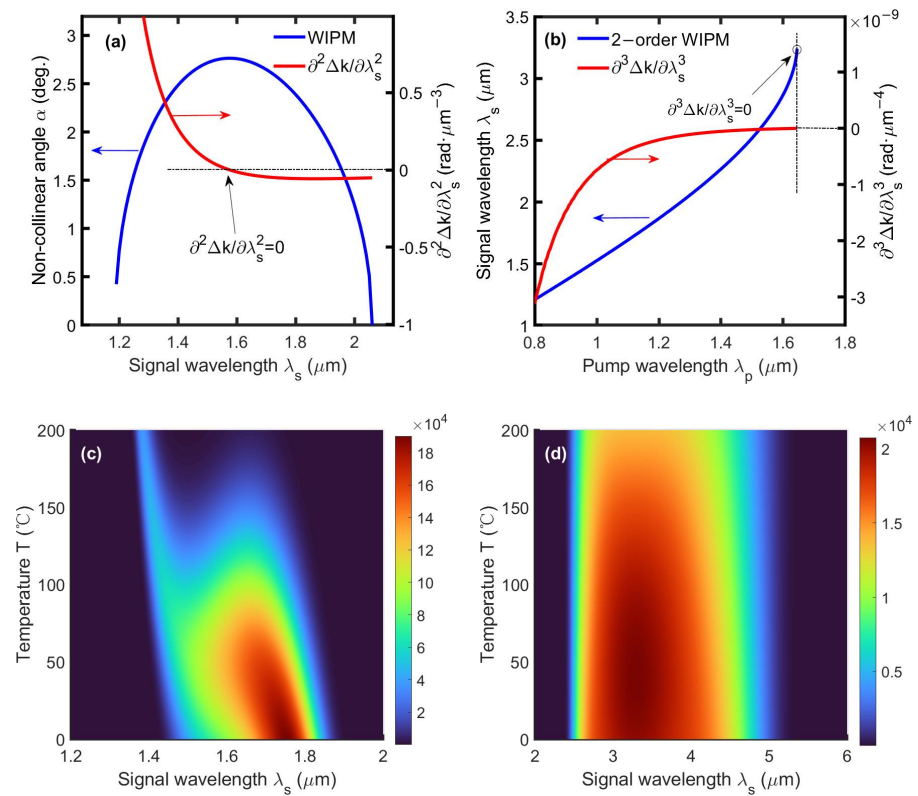
Figure 4. (**a**) Dispersion of $\partial^2 \Delta k/\partial \lambda_s^2$ (red curve) and the noncollinear angle for WIPM (blue curve) in a LiGaS$_2$-based OPA with $\lambda_p = 1.03$ μm, $T_0 = 323$ K. $\partial^2 \Delta k/\partial \lambda_s^2 = 0$ at $\lambda_s = 1.6$ μm, corresponding to the second-order WIPM ($\theta = 38.2°$, $\varphi = 0°$, and $d_{eff} = 3.6$ pm·V^{-1}). (**b**) Signal wavelength for the second-order WIPM (blue curve) and $\partial^3 \Delta k/\partial \lambda_s^3$ (red curve) versus pump wavelength. $\partial^3 \Delta k/\partial \lambda_s^3 = 0$ at $\lambda_p = 1.65$ μm and $\lambda_s = 3.3$ μm, corresponding to the third-order WIPM ($\theta = 54.1°$, $\varphi = 0°$, and $d_{eff} = 4.7$ pm·V^{-1}). (**c**) Small-signal gain as a function of signal wavelength and temperature around the second-order WIPM point in (**a**) under crystal length $L = 10$ mm and peak pump intensity $I_p = 5$ GW·cm^{-2}. (**d**) Small-signal gain as a function of signal wavelength and temperature around the third-order WIPM point in (**b**) under crystal length $L = 10$ mm and peak pump intensity $I_p = 5$ GW·cm^{-2}.

3. Numerical Simulation and Discussion

3.1. Simulation Code

Different from the theoretical analysis shown in Section 2, here, we try to evaluate the performance of the above WTIPM solutions in mid-IR OPCPA through numerical simulations: one is the strict WTIPM solution at λ_p = 2.06 μm and λ_s = 5 μm, while the other is the approximate WTIPM solution at λ_p = 1.65 μm and λ_s = 3.3 μm, which in fact is a solution of third-order WIPM. Both solutions belong to the Type-I PM in the XZ plane of LiGaS$_2$ crystal, but the former one is a noncollinear solution and the latter is a collinear solution. In this section, we consider the effects of dispersion, walk-off, diffraction, absorption, and Gaussian pulse and beam profiles. Under the slowly varying envelope approximation, the coupled-wave equations that govern the mid-IR OPCPA are as follows [31],

$$\frac{\partial A_i}{\partial z} + \rho_i \frac{\partial A_i}{\partial x} - \frac{j}{2k_i}\left(\frac{\partial^2 A_i}{\partial x^2} + \frac{\partial^2 A_i}{\partial y^2}\right) + \sum_{n=1}^{6} \frac{j^{n-1}}{n!}\gamma_{ni}\frac{\partial^n A_i}{\partial t^n} = -j\frac{\omega_i d_{eff}}{n_i c}A_s^* A_p e^{-j\Delta k_0 z} - \frac{\eta_i}{2}A_i, \quad (7)$$

$$\frac{\partial A_s}{\partial z} - \frac{j}{2k_s}\left(\frac{\partial^2 A_s}{\partial x^2} + \frac{\partial^2 A_s}{\partial y^2}\right) + \sum_{n=1}^{6} \frac{j^{n-1}}{n!}\gamma_{ns}\frac{\partial^n A_s}{\partial t^n} = -j\frac{\omega_s d_{eff}}{n_s c}A_i^* A_p e^{-j\Delta kz} - \frac{\eta_s}{2}A_s, \quad (8)$$

$$\frac{\partial A_p}{\partial z} + \rho_p \frac{\partial A_p}{\partial x} - \frac{j}{2k_p}\left(\frac{\partial^2 A_p}{\partial x^2} + \frac{\partial^2 A_p}{\partial y^2}\right) + \sum_{n=1}^{6} \frac{j^{n-1}}{n!}\gamma_{np}\frac{\partial^n A_p}{\partial t^n} = -j\frac{\omega_p d_{eff}}{n_p c}A_s A_i e^{j\Delta k_0 z} - \frac{\eta_p}{2}A_p, \quad (9)$$

where A_m is the complex envelope, ρ_i (4.8° for strict WTIPM and 0° for third-order WIPM) is the intersection angle between k_s and k_i, ρ_p (4.0° for strict WTIPM and 1.1° for third-order WIPM) is the sum of the intersection angle and walk-off angle, and $\gamma_{nm} = \partial k_m^n/\partial \omega_m^n$ is the n-order dispersion coefficient. η_m is the intensity absorption coefficient for wave m (m = s, i, and p, referring to the signal, idler, and pump, respectively), which can be obtained from Figure 1a (e.g., 0.45 cm^{-1} at 1.65 μm, 0.47 cm^{-1} at 2.06 μm, 0.23 cm^{-1} at 3.4 μm, and 0.18 cm^{-1} at 5 μm). The signal transmits along the longitudinal direction z, while x and y mark the two transverse directions. The walk-off is assumed to occur in the XZ plane for the three waves.

The absorption of three waves will heat the crystal, and the heat will be conducted from the crystal center to surroundings. In our simulations, we assumed that the crystal's lateral surface was in good contact with a heat sink of constant temperature (T_0 = 293 K), while the two end surfaces were directly exposed to air (T_{air} = 293 K). The temperature distribution in the crystal was determined by a heat transfer equation and boundary conditions [32]:

$$\nabla^2 T = \frac{\eta_p I_p + \eta_s I_s + \eta_i I_i}{\kappa}, \quad (10)$$

$$\kappa \frac{\partial T}{\partial r}\bigg|_{r=\sigma} = h_1(T_{r=\sigma} - T_0), \quad (11)$$

$$\kappa \frac{\partial T}{\partial z}\bigg|_{z=0,L} = h_2(T_{z=0,L} - T_{air}), \quad (12)$$

where κ = 6 W·(m·K)$^{-1}$ [33] is the thermal conductivity, h_1 = 400 W·m^{-2}·K^{-1} [10] is the assumed heat convection coefficient between the crystal and a copper heat sink (the temperature of crystal's lateral face will be fixed at 293 K if h_1 is large enough), h_2 = 10 W·m^{-2}·K^{-1} [34] is the heat convection coefficient between the crystal and the air, I_m is the pulse intensity of light m, σ = 7.5 mm is the radius of a round crystal aperture, and L is the crystal length. A LiGaS$_2$ crystal with a size of Φ15 × 12 mm^3 is commercially available now, and larger sizes have been reported in the literature [8,35]. Due to the moderate nonlinear coefficient, two relatively long crystals of 10.5 mm and 8 mm were chosen for the two simulation examples in Section 3.2, respectively, where the peak signal efficiency could be achieved. The seeded mid-IR signal was assumed to have a bandwidth equal to the

gain bandwidth of each solution given in Section 2 (i.e., $\Delta\lambda$ = 1 μm for strict WTIPM and $\Delta\lambda$ = 2.1 μm for third-order WIPM), which is large enough to measure the amplification bandwidth of OPCPA. This broadband seed was chirped into a Gaussian pulse with a pulse duration of 10 ps (FWHM) and a beam radius of 5 mm (FWHM). The pump had the same pulse and beam profiles as the chirped signal. Before OPA, the peak intensities of the pump and chirped signal pulses were 5 GW·cm^{-2} and 0.05 GW·cm^{-2}, respectively.

The coupled-wave equations (Equations (7)–(9)) were solved by the split-step Fourier transform and fourth-order Runge−Kutta methods, while the thermal transfer equations (Equations (10)–(12)) were solved by the finite difference method. Calculations of coupled-wave and thermal transfer equations were conducted in an alternating manner until a stable temperature distribution in the crystal was reached.

3.2. Results and Discussion

In our simulations, the signal and pump were assumed to have the same repetition rates and their pulse energies were fixed at 0.15 mJ and 15 mJ, respectively. The heat load depended on the repetition rate. Due to the lack of experimental data on the allowable tensile stress or fracture temperature for the LiGaS$_2$ crystal, here, we controlled the temperature difference within the crystal with a maximum of 100 K. Therefore, the pulse repetition rate was set at 5 kHz, corresponding to a pump power of 75 W. In the following, we conducted the simulation by assuming a constant temperature of 293 K in the lateral face of crystal (equivalently, h_1 is infinite), and also presented the efficiency evolutions along the crystal under h_1 = 400 W·m^{-2}·K^{-1} for comparison.

The strict WTIPM solution at λ_p = 2.06 μm and λ_s = 5 μm, as shown in Figure 3a, was simulated first. A signal with a very broad signal spectrum around 5 μm was seeded (black curve in Figure 5c). Figure 5a shows the temperature distribution within the crystal. The maximum temperature appeared at the front of the crystal because the absorption of the 2.06 μm pump light was larger than for the signal and idler (Figure 1a). With the depletion of the pump light, the temperature in the crystal center decreased from 390 K (front surface) to 357 K (back surface). Figure 5b shows the evolution of the conversion efficiency within the crystal. The signal efficiency grew at first and then dropped after reaching a peak of ~12% at L = 10.5 mm (red curve in Figure 5b). The conversion efficiency was lower than the quantum-limited efficiency of ~40% due to the Gaussian pulse profiles and the inherent back conversion effect [36]. In order to judge the influence of the thermal effect on the conversion efficiency, we also simulated the same OPCPA process under h_1 = 400 W·m^{-2}·K^{-1} (pink curve in Figure 5b) and without considering the crystal absorption (blue curve in Figure 5b). The three efficiency curves overlapped quite well, suggesting that the temperature increase in the crystal had almost no effect on the conversion efficiency. Such behavior can be expected from the large temperature bandwidth of WTIPM solutions. The simulated signal spectra with and without considering the thermal effect were also identical and close to the calculated small-signal gain profile, as shown in Figure 5c. Such a spectral bandwidth was comparable or even larger than that reported in 5 μm OPCPA with ZnGeP$_2$ crystals [16,17]. After compression, the amplified mid-IR spectrum supported a pulse duration of 59 fs (Figure 5d), corresponding to about 3.5 cycles at 5 μm.

The simulation results achieved for OPCPA with the third-order WIPM solution of λ_p = 1.65 μm and λ_s = 3.3 μm are shown in Figure 6a–d. Due to the similar absorption of the pump, signal, and idler, the temperature distribution within the crystal (Figure 6a) resembled that shown in Figure 5a. The peak conversion efficiency in this case (Figure 6b) was larger than that in Figure 5b due to the larger quantum efficiency. As the third-order WIPM solution is not a strict WTIPM solution, the thermal effect had some influence on the conversion efficiency, especially in the case of h_1 = 400 W·m^{-2}·K^{-1} (Figure 6b). The narrowing of the amplified signal spectrum due to the thermal effect was minor and insignificant (Figure 6c). The large amplification bandwidth from the third-order WIPM supported a shorter pulse of ~16 fs (Figure 6d), corresponding to sub-two cycles at 3.3 μm.
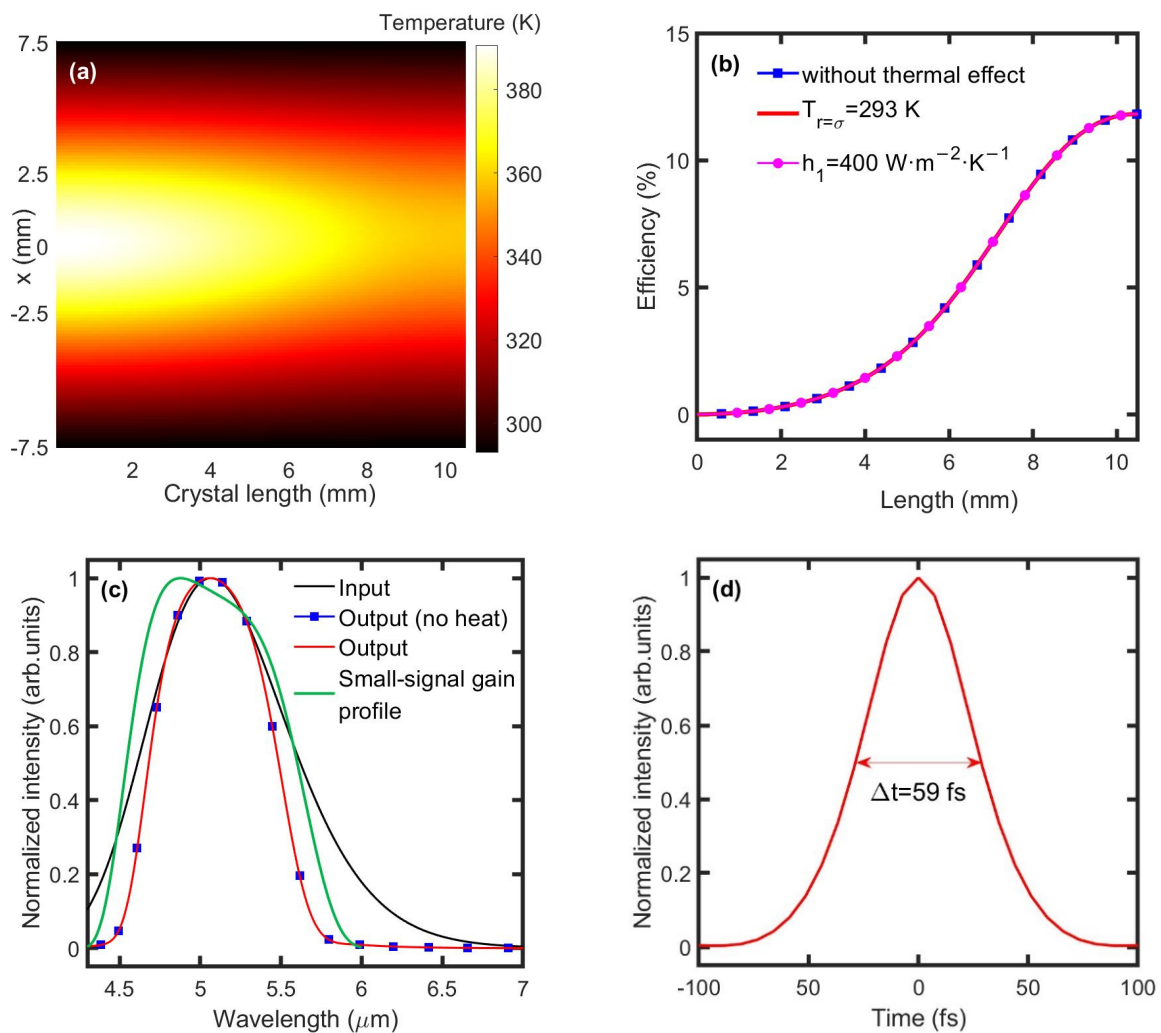
Figure 5. Simulation results for mid-IR OPCPA with WTIPM given in Figure 3a. The lateral surface of the crystal is assumed with a constant temperature of 293 K. (**a**) Temperature distribution in the xz plane of the crystal. (**b**) Conversion efficiency versus crystal length with (red) and without (blue) considering the thermal effect. Pink, the crystal's lateral surface contacts with a heat sink of constant temperature 293 K under $h_1 = 400$ W·m^{-2}·K^{-1}. (**c**) Signal spectra before OPCPA (black) and after OPCPA with (red) and without (blue) considering the thermal effect. The small-signal gain profile with $L = 10$ mm is shown as a green curve. (**d**) Compressed pulse profile.

　　The amplified mid-IR few-cycle pulses in the above two cases reached ~9 W in average power. Due to the adoption of WTIPM, the thermal dephasing effect was suppressed significantly, as shown in Figures 5 and 6. Note that the absorption coefficients adopted in the simulations were much larger than some of the recently reported results [34], so a higher average power could be expected to be achieved by using a high-quality LiGaS$_2$ crystal with a lower absorption. The average power scalability of mid-IR OPCPA was ultimately limited by the thermal cracking of LiGaS$_2$ crystal, which should be verified experimentally in the future.
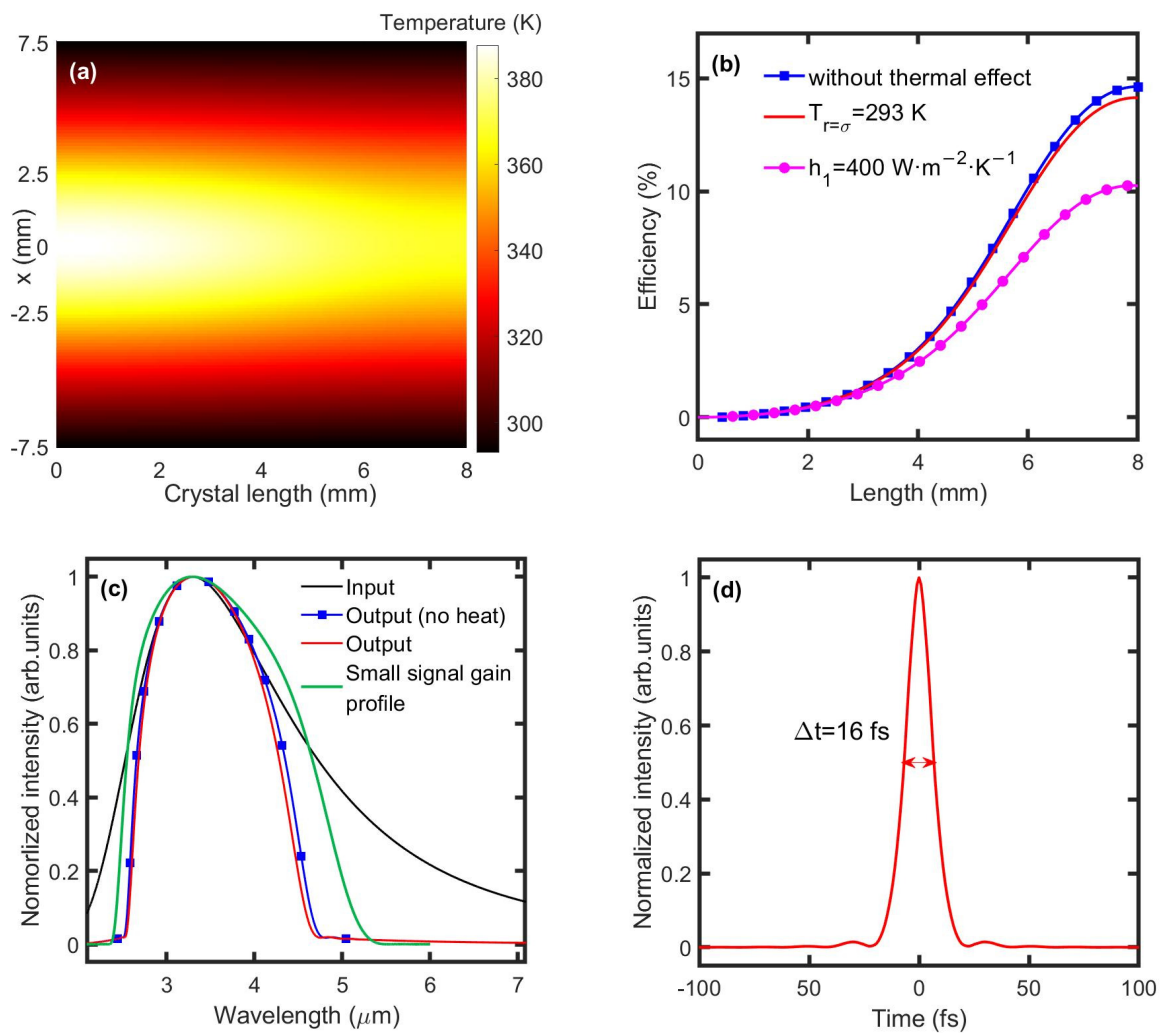
Figure 6. Simulation results for mid-IR OPCPA with the third-order WIPM given in Figure 4b. The lateral surface of the crystal is assumed with a constant temperature of 293 K. (**a**) Temperature distribution in the xz plane of the crystal. (**b**) Conversion efficiency versus crystal length with (red) and without (blue) considering the thermal effect. Pink, the crystal's lateral surface is in contact with a heat sink with a constant temperature of 293 K under $h_1 = 400$ W·m^{-2}·K^{-1}. (**c**) Signal spectra before OPCPA (black) and after OPCPA with (red) and without (blue) considering the thermal effect. Small-signal gain profile with $L = 8$ mm is shown as a green curve. (**d**) Compressed pulse profile.

4. Conclusions

In summary, we studied mid-IR OPA with simultaneous wavelength and temperature insensitivity in a LiGaS$_2$ crystal through theoretical analysis and numerical simulations. A strict WTIPM solution of $\lambda_s = 5$ μm and $\lambda_p = 2.06$ μm was found in noncollinear Type-I OPA in the XZ plane of the LiGaS$_2$ crystal; this could be tuned by varying the pump wavelength. Such a WTIPM solution can support 3.5-cycle 5 μm OPCPA with a temperature bandwidth beyond 200 K. In addition to the strict WTIPM solutions, two collinear WIPM solutions with large temperature bandwidths were also discovered for the Type-I OPA in the XZ plane of LiGaS$_2$ crystal: one was the first-order WIPM solution of $\lambda_s = 4.12$ μm and $\lambda_p = 2.06$ μm, and the other was the third-order WIPM solution of $\lambda_s = 3.3$ μm and $\lambda_p = 1.65$ μm. The two collinear solutions with a large temperature bandwidths could be treated as approximate WTIPM solutions, and the third-order WIPM solution was numerically verified for building a sub-two-cycle 3.3 μm OPCPA. The WTIPM solutions given in this study will pave the way towards achieving high-power ultrafast mid-IR OPA and OPCPA with the semiconductor LiGaS$_2$ crystal.

References

1. Wolter, B.; Pullen, M.G.; Baudisch, M.; Sclafani, M.; Hemmer, M.; Senftleben, A.; Schröter, C.D.; Ullrich, J.; Moshammer, R.; Biegert, J. Strong-Field Physics with Mid-IR Fields. *Phys. Rev. X* **2015**, *5*, 021034. [CrossRef]
2. Koç, A.; Hauf, C.; Woerner, M.; von Grafensteın, L.; Ueberschaer, D.; Bock, M.; Griebner, U.; Elsaesser, T. Compact high-flux hard X-ray source driven by femtosecond mid-infrared pulses at a 1 kHz repetition rate. *Opt. Lett.* **2021**, *46*, 210–213. [CrossRef] [PubMed]
3. Pires, H.; Baudisch, M.; Sanchez, D.; Hemmer, M.; Biegert, J. Ultrashort pulse generation in the mid-IR. *Prog. Quantum Electron.* **2015**, *43*, 1–30. [CrossRef]
4. Seidel, M.; Xiao, X.; Hussain, S.A.; Arisholm, G.; Hartung, A.; Zawilski, K.T.; Schunemann, P.G.; Habel, F.; Trubetskov, M.; Pervak, V.; et al. Multi-watt, multi-octave, mid-infrared femtosecond source. *Sci. Adv.* **2018**, *4*, eaaq1526. [CrossRef]
5. Tian, K.; He, L.; Yang, X.; Liang, H. Mid-Infrared Few-Cycle Pulse Generation and Amplification. *Photonics* **2021**, *8*, 290. [CrossRef]
6. Petrov, V. Frequency down-conversion of solid-state laser sources to the mid-infrared spectral range using non-oxide nonlinear crystals. *Prog. Quantum Electron.* **2015**, *42*, 1–106. [CrossRef]
7. Nikogosyan, D.N. *Nonlinear Optical Crystals: A Complete Survey*; Springer Science & Business Media: New York, NY, USA, 2006.
8. Yelisseyev, A.P.; Starikova, M.K.; Korolev, V.V.; Isaenko, L.I.; Lobanov, S.I. Photoluminescence of lithium thiogallate $LiGaS_2$. *J. Opt. Soc. Am. B* **2012**, *29*, 1003–1011. [CrossRef]
9. Rothhardt, J.; Demmler, S.; Hädrich, S.; Peschel, T.; Limpert, J.; Tünnermann, A. Thermal effects in high average power optical parametric amplifiers. *Opt. Lett.* **2013**, *38*, 763–765. [CrossRef]
10. Prandolini, M.J.; Riedel, R.; Schulz, M.; Hage, A.; Höppner, H.; Tavella, F. Design considerations for a high power, ultrabroadband optical parametric chirped-pulse amplifier. *Opt. Express* **2014**, *22*, 1594–1607. [CrossRef]
11. Chen, B.-H.; Wittmann, E.; Morimoto, Y.; Baum, P.; Riedle, E. Octave-spanning single-cycle middle-infrared generation through optical parametric amplification in $LiGaS_2$. *Opt. Express* **2019**, *27*, 21306–21318. [CrossRef] [PubMed]
12. Qu, S.; Liang, H.; Liu, K.; Zou, X.; Li, W.; Wang, Q.J.; Zhang, Y. 9 μm few-cycle optical parametric chirped-pulse amplifier based on $LiGaS_2$. *Opt. Lett.* **2019**, *44*, 2422–2425. [CrossRef] [PubMed]
13. Liu, K.; Liang, H.; Wang, L.; Qu, S.; Lang, T.; Li, H.; Wang, Q.J.; Zhang, Y. Multimicrojoule GaSe-based midinfrared optical parametric amplifier with an ultrabroad idler spectrum covering 4.2–16 μm. *Opt. Lett.* **2019**, *44*, 1003–1006. [CrossRef] [PubMed]
14. Heiner, Z.; Petrov, V.; Mero, M. Efficient, sub-4-cycle, 1-μm-pumped optical parametric amplifier at 10 μm based on $BaGa_4S_7$. *Opt. Lett.* **2020**, *45*, 5692–5695. [CrossRef] [PubMed]
15. Nam, S.-H.; Fedorov, V.; Mirov, S.; Hong, K.-H. Octave-spanning mid-infrared femtosecond OPA in a $ZnGeP_2$ pumped by a 2.4 μm Cr:ZnSe chirped-pulse amplifier. *Opt. Express* **2020**, *28*, 32403–32414.
16. Kanai, T.; Malevich, P.; Kangaparambil, S.S.; Ishida, K.; Mizui, M.; Yamanouchi, K.; Hoogland, H.; Holzwarth, R.; Pugzlys, A.; Baltuska, A. Parametric amplification of 100 fs mid-infrared pulses in $ZnGeP_2$ driven by a Ho:YAG chirped-pulse amplifier. *Opt. Lett.* **2017**, *42*, 683–686. [CrossRef] [PubMed]
17. von Grafenstein, L.; Bock, M.; Ueberschaer, D.; Escoto, E.; Koç, A.; Zawilski, K.; Schunemann, P.; Griebner, U.; Elsaesser, T. Multi-millijoule, few-cycle 5 μm OPCPA at 1 kHz repetition rate. *Opt. Lett.* **2020**, *45*, 5998–6001. [CrossRef] [PubMed]
18. Badikov, V.; Badikov, D.; Shevyrdyaeva, G.; Tyazhev, A.; Marchev, G.; Panyutin, V.; Noack, F.; Petrov, V.; Kwasniewski, A. $BaGa_4S_7$: Wide-bandgap phase-matchable nonlinear crystal for the mid-infrared. *Opt. Mater. Express* **2011**, *1*, 316–320. [CrossRef]
19. Petrov, V.; Yelisseyev, A.; Isaenko, L.; Lobanov, S.; Titov, A.; Zondy, J.-J. Second harmonic generation and optical parametric amplification in the mid-IR with orthorhombic biaxial crystals $LiGaS_2$ and $LiGaSe_2$. *Appl. Phys. B* **2004**, *78*, 543–546. [CrossRef]
20. Isaenko, L.I.; Yelisseyev, A.P. Recent studies of nonlinear chalcogenide crystals for the mid-IR. *Semicond. Sci. Technol.* **2016**, *31*, 123001. [CrossRef]
21. Manzoni, C.; Cerullo, G. Design criteria for ultrafast optical parametric amplifiers. *J. Opt.* **2016**, *18*, 103501. [CrossRef]
22. Guo, X.; Wang, C.; Leng, Y.; Li, R. Bandwidth analysis of type-I optical parametric chirped pulse amplification systems. *J. Opt. Soc. Am. B* **2014**, *31*, 2615. [CrossRef]

23. Hongjun, L.; Wei, Z.; Guofu, C.; Yishan, W.; Zhao, C.; Chi, R. Investigation of spectral bandwidth of optical parametric amplification. *Appl. Phys. B* **2004**, *79*, 569–576. [CrossRef]

24. Schimpf, D.N.; Rothhardt, J.; Limpert, J.; Tünnermann, A.; Hanna, D.C. Theoretical analysis of the gain bandwidth for noncollinear parametric amplification of ultrafast pulses. *J. Opt. Soc. Am. B* **2007**, *24*, 2837–2846. [CrossRef]

25. Dabu, R. Very broad gain bandwidth parametric amplification in nonlinear crystals at critical wavelength degeneracy. *Opt. Express* **2010**, *18*, 11689–11699. [CrossRef] [PubMed]

26. Tang, D.; Ma, J.; Wang, J.; Zhou, B.; Xie, G.; Yuan, P.; Zhu, H.; Qian, L. Temperature- and wavelength-insensitive parametric amplification enabled by noncollinear achromatic phase-matching. *Sci. Rep.* **2016**, *6*, 36059. [CrossRef] [PubMed]

27. Zhong, H.; Dai, D.; Dai, S.; Hu, B.; Li, Y.; Fan, D. Comprehensive analyses of the thermal insensitive noncollinear phase-matching for power scalable parametric amplifications. *Opt. Express* **2018**, *26*, 23675–23688. [CrossRef] [PubMed]

28. Dai, D.; Liang, C.; Liang, Z.; Wang, B.; Zhong, H.; Li, Y.; Fan, D. Temperature-insensitive broadband optical parametric chirped pulse amplification based on a tilted noncollinear QPM design. *Opt. Express* **2020**, *28*, 57–70. [CrossRef] [PubMed]

29. Kato, K.; Umemura, N.; Isaenko, L.; Lobanov, S.; Vedenyapin, V.; Miyata, K.; Petrov, V. Thermo-optic dispersion formula for LiGaS$_2$. *Appl. Opt.* **2019**, *58*, 1519–1521. [CrossRef] [PubMed]

30. SNLO Is a Public Domain Software. Available online: http://www.as-photonics.com/SNLO/ (accessed on 1 February 2022).

31. Yin, Z.; Ma, J.; Wang, J.; Yuan, P.; Xie, G.; Qian, L. Quasi-Parametric Chirped-Pulse Amplification Simultaneously Enables High Peak Power and High Average Power. *IEEE Photonics J.* **2019**, *11*, 1503612. [CrossRef]

32. Sabaeian, M.; Mousave, L.; Nadgaran, H. Investigation of thermally-induced phase mismatching in continuous-wave second harmonic generation: A theoretical model. *Opt. Express* **2010**, *18*, 18732–18743. [CrossRef]

33. Isaenko, L.; Yelisseyev, A.; Lobanov, S.; Krinitsin, P.; Petrov, V.; Zondy, J.-J. Ternary chalcogenides LiBC$_2$ (B = In, Ga; C = S, Se, Te) for mid-IR nonlinear optics. *J. Non-Cryst. Solids* **2006**, *352*, 2439–2443. [CrossRef]

34. Namboodiri, M.; Luo, C.; Indorf, G.; Golz, T.; Grguraš, I.; Buss, J.H.; Schulz, M.; Riedel, R.; Prandolini, M.J.; Laarmann, T. Optical properties of Li-based nonlinear crystals for high power mid-IR OPCPA pumped at 1 µm under realistic operational conditions. *Opt. Mater. Express* **2021**, *11*, 231–239. [CrossRef]

35. Atuchin, V.; Isaenko, L.; Kesler, V.; Lobanov, S. Core level photoelectron spectroscopy of LiGaS$_2$ and Ga–S bonding in complex sulfides. *J. Alloys Compd.* **2010**, *497*, 244–248. [CrossRef]

36. Ma, J.; Wang, J.; Yuan, P.; Xie, G.; Xiong, K.; Tu, Y.; Tu, X.; Shi, E.; Zheng, Y.; Qian, L. Quasi-parametric amplification of chirped pulses based on a Sm^{3+}-doped yttrium calcium oxyborate crystal. *Optica* **2015**, *2*, 1006–1009. [CrossRef]